

Structural Investigation of Bulk and Dispersed Inverse Lyotropic Hexagonal Liquid Crystalline Phases of Eicosapentaenoic Acid Monoglyceride

Anan Yaghmur, Sabah Al-Hosayni, Heinz Amenitsch, and Stefan Salentinig

Langmuir, **Just Accepted Manuscript** • DOI: 10.1021/acs.langmuir.7b03078 • Publication Date (Web): 14 Nov 2017

Downloaded from <http://pubs.acs.org> on November 20, 2017

Just Accepted

“Just Accepted” manuscripts have been peer-reviewed and accepted for publication. They are posted online prior to technical editing, formatting for publication and author proofing. The American Chemical Society provides “Just Accepted” as a free service to the research community to expedite the dissemination of scientific material as soon as possible after acceptance. “Just Accepted” manuscripts appear in full in PDF format accompanied by an HTML abstract. “Just Accepted” manuscripts have been fully peer reviewed, but should not be considered the official version of record. They are accessible to all readers and citable by the Digital Object Identifier (DOI®). “Just Accepted” is an optional service offered to authors. Therefore, the “Just Accepted” Web site may not include all articles that will be published in the journal. After a manuscript is technically edited and formatted, it will be removed from the “Just Accepted” Web site and published as an ASAP article. Note that technical editing may introduce minor changes to the manuscript text and/or graphics which could affect content, and all legal disclaimers and ethical guidelines that apply to the journal pertain. ACS cannot be held responsible for errors or consequences arising from the use of information contained in these “Just Accepted” manuscripts.



Structural Investigation of Bulk and Dispersed Inverse Lyotropic Hexagonal Liquid Crystalline Phases of Eicosapentaenoic Acid Monoglyceride

Anan Yaghmur^{1,*}, Sabah Al-Hosayni¹, Heinz Amenitsch², Stefan Salentinig³

¹*Department of Pharmacy, Faculty of Health and Medical Sciences, University of Copenhagen,*

Universitetsparken 2, DK-2100 Copenhagen Ø, Denmark

²*Elettra-Sincrotrone Trieste, Strada Statale 14, 34149 Basovizza, Trieste, Italy*

³*Laboratory for Biointerfaces, Empa, Swiss Federal Laboratories for Materials Science and*

Technology, Lerchenfeldstrasse 5, 9014 St. Gallen, Switzerland

* **Corresponding Author:** e-mail address: anan.yaghmur@sund.ku.dk

ABSTRACT: Recent studies demonstrated the potential therapeutic use of newly synthesized omega-3 (ω -3) polyunsaturated fatty acid (PUFA) monoglycerides owing to their beneficial health effects in various disorders including cancer and inflammation diseases. To date, the research was mainly focused on exploring the biological effects of these functional lipids. However, to the best of our knowledge, there is no report on the hydration-mediated self assembly of these lipids that leads to the formation of nanostructures, which are attractive for use as vehicles for the delivery of drugs and functional foods. In the present study, we investigated the temperature-composition phase behaviour of eicosapentaenoic acid monoglyceride (MAG-EPA), which is one of the most investigated ω -3 PUFA monoglycerides, during a heating-cooling cycle in the temperature range of 5-60 °C. Experimental synchrotron small-angle X-ray scattering (SAXS) evidence on the formation of a dominant inverse hexagonal (H_2) lyotropic liquid crystalline phase and its temperature-induced transition to an inverse micellar solution (L_2 phase) is presented for the fully hydrated bulk MAG-EPA system and its corresponding dispersion. We produced colloidal MAG-EPA hexosomes with an internal inverse hexagonal (H_2) lyotropic crystalline phase in the presence of F127, a well-known polymeric stabilizer, or citrem, which is a negatively charged food-grade emulsifier. In this work, we report also on the formation of MAG-EPA hexosomes by vortexing MAG-EPA in excess aqueous medium containing F127 at room temperature. This low-energy emulsification method is different than most reported studies in the literature that have demonstrated the need for using a high-energy input during the emulsification step or adding an organic solvent for the formation of such colloidal non-lamellar liquid crystalline dispersions. The designed nanoparticles hold promise for future drug and functional food delivery applications due to their unique structural properties and the potential health-promoting effects of MAG-EPA.

1
2
3
4 **1. INTRODUCTION**
5

6 Long-chain omega-3 (ω -3) polyunsaturated fatty acids (PUFAs) are among the most investigated
7 nutritional compounds with health-promoting effects.¹⁻⁷ These essential fatty acids are not
8 endogenously synthesized in the body and must be provided through the diet.^{3,5} Most ω -3 PUFA
9 studies have focused on eicosapentaenoic acid (EPA; 20:5 n-3) and docosahexaenoic acid (DHA;
10 22:6 n-3), which are typically found in seafood and different fish oil supplements and products.^{2,3,5}
11 ω -3 PUFAs display positive health-promoting effects for cancer, angiogenesis, cardiovascular
12 diseases (CVD), cognitive decline, inflammation, and depression, among others, as demonstrated in
13 several epidemiological, pre-clinical and clinical studies.¹⁻⁸ In particular, there is an important role
14 of high intake of ω -3 PUFAs in anti-inflammatory processes and in the prevention of CVD.^{1-3,5,8}
15 Ingestion of EPA and DHA is well known to lower the risk of CVD *via* reduction of serum
16 triacylglycerols (TAG).¹ The American Heart Association (AHA) recommends therefore a daily
17 consumption between 200 and 500 mg of EPA and DHA for preventing coronary diseases, and this
18 may be accomplished by eating fish (preferably oil fish) at least twice a week.^{1,2,4,9} However, fish
19 and seafood contamination with toxins, polychlorinated biphenyls (PCB), and other environmental
20 pollutants may lead to risks to health.¹⁰ This necessitates the need to design applicable safe and
21 efficient ω -3 PUFA-delivery systems.
22

23
24 Despite the critical role of ω -3 PUFAs in human health and nutrition, the high susceptibility to an
25 oxidative degradation during storage, processing, and transport due to the presence of poly double
26 bonds in their carbon backbone, the poor solubility in water, and rapid elimination and clearance
27 from the body remain major problems that restrict their use for pharmaceutical applications.^{1,2,4} To
28 address these challenges, several approaches for achieving efficient delivery and improving
29 oxidative stability of EPA, DHA and other important poorly water soluble nutraceuticals have been
30 proposed in designing functional food and drug micro- and nano-carriers for the maintenance of the
31
32
33
34
35
36
37
38
39
40
41
42
43
44
45
46
47
48
49
50
51
52
53
54
55
56
57
58
59
60

well-being and also for different therapeutic purposes.^{2,11,12} Different formulations including liposomes, emulsions, and micelles have been tested for loading EPA, DHA.

It is interesting that ω -3 PUFA supplements are not only available in free fatty acid, triglyceride, ethyl ester, and phospholipid-enriched forms^{5,13-16} but they are also available as reported in recent studies in the form of monoglycerides (monoacylglycerols): eicosapentaenoic acid (MAG-EPA), docosahexaenoic acid (MAG-DHA), docosapentaenoic acid (MAG-DPA) monoglycerides, respectively.¹⁷⁻¹⁹ These novel ω -3 PUFA monoglycerides are synthesized by esterification of EPA, DHA, and DPA in the *sn*-1 position of glycerol and possess anti-inflammatory and anti-proliferative properties, which may exert beneficial health effects in various disorders including rheumatoid arthritis, chronic airway inflammatory events, pulmonary hypertension, and lung adenocarcinoma.¹⁷⁻²⁶ In addition, they are safe, stable precursors that can be hydrolysed and metabolized to produce corresponding EPA, DHA, and DPA derivatives.¹⁷⁻¹⁹ These generated bioactive metabolites are able to mediate different immune-modulatory effects through activation of specific receptors and to blunt therefore inflammatory events and reverse angiogenic and hyper-responsiveness in numerous diseases.^{19,23} It was also reported that the intestinal absorption of these ω -3 PUFA monoglycerides does not require pancreatic lipase, and therefore their behaviour is different than the corresponding ω -3 triacylglycerides (TAG- ω 3), which have to be converted through hydrolysis to free fatty acids and monoglycerides prior to absorption.^{19,27} It has also been demonstrated in recent studies that ω -3 PUFA monoglycerides have better absorption capacity than the corresponding free PUFAs and they increase the bioavailability of ω -3 PUFAs as compared to TAG- ω 3 and ω -3 PUFA-containing ethyl esters.^{17-19,28} The molecular structures of EPA, DHA, DPA, and the corresponding amphiphilic compounds MAG-EPA, MAG-DHA, and MAG-DPA are presented in **Figure 1**.

In various studies, monoglycerides of oleic (MO), elaidic (ME), and linoleic acid (MLO) have been demonstrated to display self-assemblies of micellar solutions and lyotropic lamellar and non-lamellar liquid crystalline phases on exposure to water.²⁹⁻³⁷ Among these monoglycerides, monoolein (MO) and monolinolein (MLO) are the most investigated surfactant-like lipids with biological relevance that display inverse lyotropic non-lamellar liquid crystalline phases on exposure to excess water at ambient temperatures.^{31,33,38-41} They are typically used as main lipid constituents of cubosomes and hexosomes, which are attractive drug and functional food nanocarriers.^{33,41-46} These nanoparticles with self-assembled interiors of inverse bicontinuous cubic (Q₂) and hexagonal (H₂) phases, respectively.³⁹⁻⁴² ω-3 PUFA monoglycerides are also attractive new main lipid constituents for producing lamellar and non-lamellar liquid crystalline phases and corresponding dispersions that hold promise for drug and functional food delivery applications. However, to the best of our knowledge, there is no report on the structural features of lyotropic liquid crystalline phases based on MAG-EPA, MAG-DHA, or MAG-DPA, and their use in the production of liquid crystalline nanoparticles. In the present work, we exclusively focus on investigating the effects of temperature and hydration on the nanostructural characteristics of self-assemblies based on MAG-EPA by using synchrotron small-angle X-ray scattering (SAXS). In addition, an integrated approach involving SAXS, cryogenic transmission electron microscopy (cryo-TEM), and Nanoparticle Tracking Analysis (NTA) was applied to gain insight into the morphological features and size characteristics of corresponding hexosomes stabilized using either the polymeric stabilizer F127 or the food-grade emulsifier citrem. This approach could potentially open a rational and affordable solution for introducing a novel platform for delivering the essential fatty acid EPA by producing nano-self-assemblies based on the monoglyceride MAG-EPA.

2. EXPERIMENTAL SECTION

2.1 Materials

Eicosapentaenoic acid monoglyceride (MAG-EPA) was received as a gift from SCF Pharma (Quebec, Canada). MAG-EPA has an acid value of about 3.7 mg KOH/g lipid and contains a small amount (about 2 wt%) of free fatty acid (FFA). This lipid was synthesized by using as starting material ethyl eicosapentaenoate (EPA ethyl ester)^{17,18}. Pluronic F127 was a gift from BASF SE (Ludwigshafen, Germany). Grinsted[®] citrem LR10, which is a citric acid ester of monoglycerides and diglycerides made from sunflower oil, was received as a gift from Danisco A/S (Copenhagen, Denmark). All ingredients were used without further purification. The water was double distilled.

2.2 Preparation of Non-Dispersed Binary MAG-EPA/Water Systems. MAG-EPA was hydrated by adding dropwise water and carrying out at least 5 freeze-thaw cycles between liquid nitrogen and room temperature and homogenizing several times during the thawing steps by vigorous vortexing. The vials of the prepared samples at different water content were flushed with nitrogen gas for 3 min, capped, covered by aluminum foil, and then incubated at 4 °C for at least one week before performing the SAXS measurements. The fully hydrated sample was formed at water concentration of 90 wt%; whereas the three samples prepared under limited hydration condition contained 5, 15, and 40 wt% water.

2.3 Aqueous MAG-EPA Dispersion Preparation. The aqueous dispersions were prepared using the polymeric stabilizer F127 or the negatively charged food-grade emulsifier citrem. F127-stabilized dispersion (sample D_{F127}) containing 5 wt% MAG-EPA, 1 wt% F127 and 94 wt% water was prepared using a high-energy emulsification technique (ultrasonication) or by applying a low-energy input during emulsification (vortexing) at room temperature for 10 min. The dispersions

based on the binary MAG-EPA/citrem mixtures containing 5 wt% MAG-EPA/citrem mixture and 95 wt% water were prepared at two different MAG-EPA/citrem weight ratios of 2:3 (sample CM2:3) and 3:2 (sample CM3:2). Application of a low-energy input during emulsification was not sufficient for enabling the formation of colloidally stable liquid crystalline nanoparticles, in contrast to F127-stabilized MAG-EPA dispersion (sample D_{F127}) that did not require a high-energy input for emulsifying MAG-EPA in excess water. The applied high-energy emulsification method for the production of the dispersions was as following: MAG-EPA or a binary MAG-EPA/citrem mixture were dispersed in excess water by means of ultrasonication (Qsonica MIS 4417 and Qsonica MIS 4659 4-tip horn (Qsonica LLC., Newtown, CT, USA), for 2 min in pulse mode (5 s pulses interrupted by 2 s breaks) at 27% of its maximum power until and stable milky solutions were obtained. The vials of all prepared samples were flushed with nitrogen gas for 3 min, capped, covered by aluminum foil, and then incubated at room temperature before performing the SAXS experiments.

2.4 Synchrotron Small Angle X-ray Scattering (SAXS). SAXS patterns were recorded at the Austrian SAXS beamline in the synchrotron light source ELETTRA (Trieste, Italy). The 2D SAXS patterns were acquired using a Pilatus3 1M detector (Dectris Ltd, Baden, Switzerland; active area 169 x 179 mm² with a pixel size of 172 μ m) and integrated into one-dimensional (1-D) scattering function $I(q)$ using Fit2D and then analyzed with IGOR pro (Wavemetrics, Inc., Lake Oswego, OR). An X-ray beam having a wavelength of 1.54 Å at an X-ray energy of 8 keV was used, with a sample to detector distance of 1314 mm covering a q -range of interest from about 0.07 to 5.0 nm⁻¹, where q is the length of the scattering vector, defined by $q = 4\pi/\lambda \sin(\theta/2)$, where λ is the wavelength and 2θ is the scattering angle. Silver behenate (CH₃-(CH₂)₂₀-COOAg with a d -spacing value of 58.38 Å)

was used as a standard to calibrate the angular scale of the measured intensity. In our investigations, 1 mm diameter quartz capillaries (sample holders) were used. The samples were thermostated with a water bath (temperature stability ± 0.1 °C, Unistat CC, Huber, Offenburg, Germany). Before carrying out the continuous temperature scan experiments, static measurements were performed at 37 °C with an exposure time of 20 s per frame with 3s delay between 5 frames. The temperature ramps in the range of 5-60 °C were programmed with scan rate of 1 °C/min typically recording every a degree an X-ray pattern. The unit cell parameters of the inverted-type hexagonal (H_2) phases were derived from the SAXS diffraction patterns. After the raw data had been corrected for detector efficiency and the background scattering, all Bragg peaks were fitted by Lorentzian distributions. We note that in each respective phase regime only the strongest reflections were considered. For the inverted micellar solution (the L_2 phase), the characteristic distance, d , was calculated.

2.5 Cryo-transmission electron microscopy (Cryo-TEM). The morphological characterization of MAG-EPA and MAG-EPA/citrem nanoparticles prepared using a high-energy emulsification was done under a frozen-hydrated state as previously described.⁴⁷ Briefly, 3-4 μ L of the dispersions were applied on a hydrophilized lacey carbon 300 mesh copper grid (Ted Pella Inc., California, USA). The excess sample on the grid was then blotted with filter paper at blotting time 5 s, blotting force 0, temperature 25 °C and 100 % humidity (FEI Vitrobot IV, Holland), and was rapidly plunged into liquid-nitrogen cooled ethane (-180 °C). The samples observation was done with Tecnai G2 20 transmission electron microscope (FEI, Holland) at a voltage of 200 kV under low-dose rate (~ 5 e/ \AA^2 s). Images were then recorded using a FEI Eagle camera 4x4 k at a nominal magnification of 69,000x resulting in a final image sampling of 0.22 nm/pixel.

2.6 Zeta Potential. The zeta potential of the dispersions were measured using a Zetasizer Nano ZS (Malvern Instruments, Worcestershire, U.K.) equipped with a 633 nm laser and 173° detection optics. Measurements were performed at room temperature on samples diluted 100x in water. Malvern DTS v. 6.34 software (Malvern instruments, Worcestershire, U.K.) was used for data acquisition and analysis. For the viscosity and refractive index, the values of pure water were used.

2.7 Nanoparticle tracking analysis (NTA). Size characterization of the dispersions was conducted at room temperature using Nanoparticle Tracking Analysis (NTA) on NanoSight NS300 (Malvern Instruments Ltd, Worcestershire, UK) mounted with a 405 nm laser. NTA takes into consideration the properties of both light scattering and Brownian motions of the nanoparticles in the determination of their size distribution. Prior to measurements, the samples were diluted 10^4 times in ultra-pure water ($18.2 \text{ M}\Omega\cdot\text{cm}$) to reach a measured concentration between 10^8 and 10^9 particles/mL and minimise interparticle interactions that would influence the measurement. All dispersions were measured in triplicate using same camera settings and analyzed under same criteria to allow direct comparison. All measurements were based on ~2000 individually detected nanoparticles from 5 to 9 videos from different locations in the sample. The recorded videos were analysed using Malvern software (NTA 3.2 Dev Build 3.2.16). Pure water was measured as a control at identical instrumental settings, and contained no detectable particles.

3. RESULTS AND DISCUSSION

3.1 Self-Assembly of Hydrated MAG-EPA into Inverse Micellar Solutions and Hexagonal Liquid Crystalline Phases. Synchrotron SAXS experiments were performed to investigate the

effect of temperature on the self-assembled nanostructures of three hydrated MAG-EPA samples during a heating-cooling cycle between 5 and 60 °C using ramp of 1 °C/min. Two of these samples containing 5 and 15 wt% water were clear and transparent solutions prepared below limiting hydration, and one sample was prepared under excess water conditions (full hydration conditions).

Figure 2 shows the temperature-dependent behaviour of these systems during the heating cycle. It is interesting that the H₂ and the L₂ phases were the only phases observed for MAG-EPA/water systems. In the temperature range of 5-27 °C, the experimental findings point out that hydration of MAG-EPA induces a clear L₂-H₂ phase transition. At 5 wt% water (**Figure 2A**), the hydration of MAG-EPA induces the formation of inverse micelles (L₂ phase); whereas the inverse hexagonal (H₂) phase was detected with increasing water content to 15 wt% (**Figure 2B**) and also under excess water conditions for the sample containing 90 wt% water (**Figure 2C**). It should be noted that a biphasic sample was obtained at 90 wt% water: fully hydrated H₂ phase as identified by SAXS coexisting with excess water. The observed structural transitions are consistent with previous research studies on the hydration-triggered formation of different self assemblies including lyotropic lamellar and non-lamellar liquid crystalline phases in binary unsaturated monoglyceride/water systems including MO/water, MLO/water, and ME/water systems.^{30,31,36,37,48-}

⁵⁰ It was found that the molecular structural features of these lipids including the acyl chain length^{36,48,51}, the unsaturation degree³¹, the double bond position⁵² and configuration in the acyl chain^{30,34}, and the size of the hydrophilic headgroup moiety^{53,54} play an important role in modulating the structural characteristics of the obtained self assemblies and mediating the anomalous phase behaviour⁵⁵. As compared with the most investigated monoglycerides MO and MLO, which tend to form an inverse bicontinuous cubic phase with space group *Pn3m* under full hydration conditions at ambient temperatures^{29,31}, MAG-EPA has propensity to form an inverse hexagonal (H₂) phase in excess water at relatively low and ambient temperatures (**Figure 2C**). The

latter was the dominant phase (**Figure 2C**), and the observed phase behaviour is similar to that reported to monoerucin⁵⁰, which is a monounsaturated monoglyceride (C22:1, c13: double bond at the position 13) with a longer acyl chain than MO (C18:1, c9) and MLO (C18:2, c6 and c9). Thus, these experimental findings show an increased preference to a more inverse interfacial curvature with increasing the acyl chain length and therefore the H₂ phase dominates in the investigated temperature range. It is well known that the tendency of monoglycerides, which is a family of amphiphilic compounds with relatively small headgroups (weakly hydrogen-bonding lipids)^{36,55,56}, to form lyotropic lamellar and non-lamellar phases is significantly affected by alterations in their acyl chain length. For instance, monoglycerides with shorter chain lengths such as monomyristolein (C14:9, c14: double bond at the position 9) have a cylindrical-shaped molecular geometry⁵⁷ and therefore prefer to form lamellar (L_α) phases in excess water; whereas monoglycerides with a relatively long chain length³⁶ such as MO, MLO, monoerucin, and MAG-EPA have a more wedge-shaped geometry and therefore tend to form in excess water non-lamellar lyotropic liquid crystalline phases (bicontinuous cubic *Pn3m* or discontinuous H₂ self-assembled nanostructures).

An additional important observation is the role of unsaturation degree in modulating the phase transition temperatures. Previous studies on MO²⁹ and MLO³¹ showed that an increased in the unsaturation degree of monoglycerides is associated with a significant decrease in the phase transition temperatures. In this context, MLO in excess water due to the presence of two double bonds³¹ in its hydrophobic backbone have *Pn3m*-H₂ and H₂-L₂ phase transition temperatures of approximately 54 °C and 94 °C, respectively. For MO in excess water²⁹, the same phase transitions occur at higher temperatures of approximately 90 and above 100 °C, respectively. Both MLO³¹ and MO²⁹ are not highly pure in these reports. The presence of relatively small amounts of additional lipids and diglycerides could also affect the *Pn3m*-H₂ and H₂-L₂ phase transition temperatures. In this respect, Mezzenga et al.⁵⁸ reported that the H₂-L₂ phase transition temperature occurs at about

90 °C for the fully hydrated commercial distilled monoglyceride Dimodan U, which is less rich with MLO (about 61.9%) and contains different monoglycerides and a residual amount of diglycerides. In the present work, there was no indication on the formation of the bicontinuous cubic $Pn3m$ phase in the investigated temperature range. For MAG-EPA in excess water, increasing the unsaturation degree as compared to MO was associated with the formation of the neat H_2 phase at relatively low temperatures and the occurrence of the H_2 - L_2 phase transition temperature at approximately 56 °C. These results suggest that increasing the unsaturation degree of monoglycerides plays an important role in the stabilization of the L_2 phase at lower temperatures than those reported for MO and MLO. This could be attributed to an increase in the fluidity of the lipid-water interfacial film with increasing the unsaturation degree.

Figure 3 presents representative SAXS patterns on the temperature-dependence of the three hydrated MAG-EPA samples during the heating-cooling cycle. At 5 wt% water, a single broad peak indicating the formation of a neat L_2 phase was detected (**Figure 3A**) and the structure was stable and only slightly affected by varying temperature (**Figure 4A**). The temperature-triggered change of the calculated characteristic distance during the heating-cooling cycle was very small and in the range of 2.84-2.92 nm. Thus, the characteristic distance changed with an almost equal rate of about 0.002 nm/°C in both heating and cooling directions. Increasing water content to 15 wt% led to the formation of H_2 phase that was stable when heating the sample in the investigated temperature range of 5-27.5 °C (**Figure 2B**). It is worth noting that a coexisting L_2 phase started to evolve at about 10 °C in the heating direction and a complete H_2 - L_2 phase transition was detected at about 28 °C. **Figure 3B** presents a representative example at 25 °C on the detection of L_2 phase coexisting with traces of the H_2 phase during the heating step. The first weak reflection of the coexisting H_2 phase appeared at $q \sim 0.22 \text{ nm}^{-1}$ and its assignment was based on investigating the temperature-dependent behaviour of the neat H_2 phase appeared at lower temperatures. Clearly, the H_2 - L_2 phase

transition temperature was lowered to about 18 °C when the sample was cooled down from 60 to 5 °C (**Figure 3B**). As suggested in various previous studies⁵⁹, this undercooling phenomenon is most likely attributed to a slow re-arrangement mode of the lipid and water molecules that require longer experimental time scales than the characteristic equilibrium times for the H₂-L₂ phase transition. In a previous review⁵⁹, Tenchov discussed the temperature-dependent behaviour of various lipid dispersions and highlighted the influence of slow re-arrangement modes during the phase transitions on the reversibility of the phase transitions and the occurrence of metastable phases during heating-cooling cycles.

The H₂ and L₂ phases were slightly affected by varying temperature (**Figure 3B**). In the heating and cooling steps (**Figure 4B**), the lattice parameter, $a(T)$, of the H₂ phase was very slightly increased from 4.16 to 4.20 nm during heating in the temperature range of 5-27.5 °C; and no change in the lattice parameter of this phase was detected during the cooling step in the temperature range of 5-17.5 °C. A very slight change in the characteristic distance of the L₂ phase in the range of about 3.55-3.60 and 3.55-3.64 nm was also obtained, respectively. It was reflected with a decrease rate of about -0.002 nm/°C during the heating step from 28 to 60 °C and an increase rate with almost same when the temperature was decreased from 60 to 18 °C. For the H₂ phase under full hydration conditions (**Figures 3C and 4C**), the $a(T)$ value dropped more significantly from 5.13 nm to 4.58 nm with a rate of about -0.012 nm/°C as the temperature increased in the range of 5-60 °C (**Figure 4C**). Cooling the sample from about 52 to 5 °C was associated with an increase in $a(T)$ of the detected H₂ phase from 4.69 nm to 5.11 nm and the rate was almost same as that obtained during heating the sample (**Figure 4C**). An additional observation is the appearance of an intermediate H₂ from about 22 °C to 54.5 °C. During heating the sample, the $a(T)$ of this phase has a similar decrease rate of about -0.012 nm/°C in the temperature range of 46-54.5 °C (**Figure 4C**). It is worth noting that the obtained decrease rates for both coexisting H₂ phases are slightly lower than the

reported values of about $-0.016 \text{ nm}/^{\circ}\text{C}$ for the fully hydrated MO at $90\text{--}100^{\circ}\text{C}$ ^{34,60} and binary MO/ME systems at $59\text{--}85^{\circ}\text{C}$ ³⁰.

The effect of temperature on the structural properties of inverse lyotropic non-lamellar liquid crystalline phases and micellar solutions based on unsaturated monoglycerides was investigated in various studies.^{29-31,33,35,37} It was reported that alterations in the structural parameters of these self assemblies and the detected structural transitions are attributed to simultaneous temperature-triggered changes in the hydration degree of the hydrophilic headgroups and the effective volume of the acyl chains of monoglycerides (thermal expansivities).^{29,31} It is expected that the temperature-triggered change in the lattice parameters of the H_2 phase under full hydration conditions (**Figure 3C**) is more significant than the phases prepared with limited hydration level (**Figure 4A and 4B**) due to the combination of increased thermal expansivities with a more pronounced dehydration effect.³¹ The typical temperature-dependent behaviour induces a transition from lamellar and inverse bicontinuous cubic phases to inverse discontinuous phases with more negative curvatures including H_2 and L_2 nanostructures in the heating step.^{29,31,36,50} Decreasing temperature exerts an opposite effect but hysteresis effects could be observed and their occurrence depends on the nature of the structural transition, and different factors including the characteristic times for hydration/dehydration of the lipid hydrophilic headgroups and re-establishment of hydrogen bonding networks.⁵⁹

An important point worth considering from the presented experimental findings is related to reversibility of structural transitions during heating-cooling cycles. In a previous study³¹, it was found that MLO in excess water forms fully reversible structural transitions with a monotonous exchange of water between the self-assemblies and the surrounding aqueous medium during the heating-cooling cycles. However in the present study, slight hysteresis effects were exhibited in the investigated temperature range, which they may arise from working under non-equilibrium

conditions. It should be noted that MLO self assemblies were left at least 600 s at the respective temperatures before SAXS characterization³¹; whereas the three selected samples in the present work were investigated in the aforementioned temperature scan without having waiting times between the performed experiments. The phase transitions of hydrated MAG-EPA are most likely similar to those of MLO and belong to the same group of fast structural transformations, known also as 'highly cooperative' phase transitions⁵⁹, which are characterized by a decrease in their small thermal hystereses with decreasing the temperature scan rate.

This study represents only a step toward the complete construction of the temperature-composition phase diagram of MAG-EPA. We are aware that the structural characterization and identification of the phases at different hydration levels and temperatures were only considered on three samples. Future studies are still needed for detailed structural analysis and complete construction of the binary MAG-EPA/water phase diagram. It is also important to shed light on the influence of the molecular structure of ω -3 PUFA monoglycerides on their phase behaviour. In particular, the structural properties of MAG-EPA in excess water should be compared with those of MAG-DHA and MAG-DPA due to the reported positive health effects of these monoglycerides and their attractiveness in the formation of nanocarriers for drug and functional food delivery applications.

3.2 Formation and Characterization of MAG-EPA Nano-Self Assemblies. Three different dispersions were prepared to shed light on the structural and morphological features of MAG-EPA nano-self-assemblies. In this study, the dispersions were stabilized with F127, a well-known efficient triblock copolymer typically used for the formation of cubosomes and hexosomes based on unsaturated monoglycerides^{31,39,61,62}, and citrem, which is an anionic food-grade emulsifier composed of citric acid esters of monoglycerides and diglycerides. The selection of citrem as a stabilizer for MAG-EPA nanoparticles was based on recent findings suggesting its potential use in

the development of hemocompatible injectable nanoparticles that do not trigger complement activation.^{47,63} The three prepared dispersions flushed with nitrogen gas were colloidally stable based on visual inspection at room temperature for at least four months after preparation. SAXS patterns for these dispersions at 37 °C are shown in **Figure 5A**. The SAXS pattern of the F127-stabilized dispersion (sample D_{F127}) has three characteristic reflections of an inverse hexagonal (H₂) phase with a lattice parameter of 4.87 nm indicating the formation of hexosomes. To investigate the effect of F127 on the internal nanostructure of the produced hexosomes at 37 °C, we compared the nanostructural features of D_{F127} with those of the non-dispersed bulk samples prepared at different water concentrations (**Figure 5B**). The identified phases and the corresponding lattice parameters of these bulk phases are given in **Table 1**. The obtained SAXS data confirm that the lattice parameter of the full hydrated bulk sample is almost the same as the corresponding internal H₂ nanostructure of the F127-stabilized hexosomes. These results are consistent with previous studies on MLO- and MO-based hexosomes^{31,53,64} and indicate that F127 is an efficient stabilizer that does not penetrate into the self-assembled interiors of the dispersed nanoparticles, but mainly adheres to their outer surfaces. An interesting aspect of retaining the same fully hydrated H₂ nanostructure in the interiors of hexosomes is the possible prediction of the solubilized water content in the internal nanostructure of hexosomes: the obtained SAXS results suggest that both dispersed and bulk (non-dispersed) fully hydrated H₂ nanostructures were able to accommodate almost same water content. It is worth mentioning in this context that MAG-EPA reached the full hydration conditions at a water concentration above 40 wt% at 37 °C. Hence, further increase of water content to 90 wt% did not affect the lattice constant of the H₂ phase under these excess water conditions (**Figure 5B**). It should be noted that we did not investigate in detail the hydration boundary of MAG-EPA at different temperatures. However, we expect that the hydration boundary of MAG-EPA will occur at lower water concentrations with increasing temperature when taking into consideration the similar

temperature-dependence of the self assemblies of MAG-EPA (**Figures 1-3**) to those reported for other unsaturated monoglycerides including MO²⁹ and MLO³¹. In this respect, the reported hydration boundaries for MO and MLO³¹ are 36% water at 40 °C and 33 wt% at 20 °C, respectively.

Citrem, in contrast to F127, as can be seen in **Figure 5A**, was not only adhered to the outer surfaces of the dispersed nanoparticles to enhance their colloidal stability in excess water but also induced structural alterations in both dispersions (samples CM2:3 and CM3:2). Increasing citrem/ MAG-EPA weight ratio from 2:3 (CM2:3) to 3:2 (CM3:2) induced a transition from hexosomes with a neat internal H₂ phase having lattice parameter of 4.91 nm (**Table 1**), which is slightly greater than the lattice parameter of the fully hydrated bulk (non-dispersed) H₂ phase, to nanoparticles enveloping an internal biphasic H₂/L₂ feature (**Figure 5A** and **Table 1**). The assignment of the coexisting L₂ phase with increasing citrem concentration was based on the detection of an additional broad peak in the SAXS pattern at $q \sim 1.42 \text{ nm}^{-1}$ (**Figure 5A**). This result is consistent with previous studies^{47,63,65-67} on the tendency of citrem to induce a transition in MO-based dispersion from hexosomes to ELP (nanoparticles with an internal L₂ phase). For instance, a similar phase transition sequence was recently detected upon increasing citrem concentration in dispersions based on binary MO/medium chain triglycerides (MCT) mixtures⁶³ and dispersions based on binary soy phosphatidylcholine/citrem mixtures⁴⁷ and was attributed to the preferential localization of citrem in the hydrophobic domains of the self-assembled interiors of the dispersed nanoparticles.^{47,63,65,66}

In addition to SAXS, cryo-TEM was used to gain insight into the morphological features of MAG-EPA nano-self-assemblies. According to the cryo-TEM images presented in **Figure 6**, the nanoparticles stabilized either with F127 (**Figure 6A**) or citrem (**Figures 6B** and **6C**) enveloped an internal nanostructure and were in the size of tens of nanometers. It was not possible to gain insight

on the structural features of the interiors of these nanoparticles seen within cryo-TEM resolution limit. Based on SAXS data analysis (**Figure 5**), these detected nanoparticles are most likely hexosomes. In addition to hexosomes, co-existing vesicles (marked with blue arrows in **Figure 6A**) were detected in the F127-stabilized dispersion. This was not surprising as they are typically observed in cubosomes and hexosomes stabilized with F127.^{31,33,61} It is interesting that the micrographs taken from the two citrem-stabilized dispersions (**Figures 6B and 6C**) did not reveal any indication on the formation of coexisting vesicles but rather smaller nanoobjects with sizes of few tens on nanometers were detected. It was not possible to identify these tiny nanoobjects and their self-assembled interiors, which were very close to the cryo-TEM resolution limit. We do not exclude that these nanoobjects include also relatively very small hexosomes.

Cryo-TEM is not a quantitative methodology for the precise determination of the nanoparticle size and size distribution. Thus, it was important to gain further insight into the size characteristics of MAG-EPA dispersions by using nanoparticle tracking analysis (NTA). For these dispersions prepared by ultrasonication, the mean and median nanoparticle sizes (nanoparticle diameters) were in the range of 82-129 and 73-115 nm, respectively (**Table 2**). For citrem-stabilized dispersions, the nanoparticles were stabilized in excess water through electrostatic stabilization mechanism and the obtained negative zeta potential values are expected and agreed well with previous reported values for emulsions, and lamellar and non-lamellar liquid crystalline nanoparticles that were stabilized by this anionic food-grade emulsifier.^{47,63,65,66,68}

3.3 Formation of MAG-EPA Nano-Self Assemblies by a Low-Energy Emulsification Method.

Various studies reported on the need to use either a high-energy emulsification method^{31,33,39,61} or a hydrotrope method⁶⁹, or their combination⁶⁹ for producing colloidally stable cubosomes and hexosomes based on unsaturated monoglycerides. To the best of our knowledge, there is no report

in the literature on the emulsification of unsaturated monoglycerides with propensity to form non-lamellar liquid crystalline phases such as MO and MLO by using a low-energy emulsification process in the absence of an organic solvent such as ethanol. In the present work, it was possible to prepare MAG-EPA hexosomes by employing a low-energy emulsification method: the nanoparticles were produced in the presence of the polymeric stabilizer F127 by simply vortexing MAG-EPA in excess water for 10 min. The mean and median nanoparticle sizes of these nanoparticles were 109.1 ± 35.5 and 93.4 ± 35.5 nm (**Table 2**). It was found that these nanoparticles are only around 25-40 nm larger than the mean and median sizes of those prepared (the values were 82.0 ± 30.3 and 72.7 ± 30.3 nm, **Table 2**) by a high energy emulsification method (ultrasonication). The production of non-lamellar liquid nanoparticles by using a low-energy emulsification method is an attractive approach, particularly for the development of nanocarriers of temperature-sensitive and solvent-labile drugs.³⁹ A major advantage of this emulsification method is the reduced risk of oxidation of ω -3 PUFAs, especially EPA. It is well known that ω -3 PUFAs are highly prone to oxidation and therefore it is attractive to produce their nanocarriers by using a simple low-energy emulsification method.

The measured negative zeta potential value for the dispersion (-22.70 mV, **Table 2**) provides the most plausible explanation for the production of MAG-EPA nanoparticles by using a low-energy emulsification method. The dispersed nanoparticles were negatively charged due most likely to the presence of negatively charged fatty acid impurities (mainly EPA) in MAG-EPA that were conferred to the nano-self-assemblies. Thus, the stabilization of these colloidal nanoparticles in excess water is most likely achieved through a combination of steric and electrostatic effects in the presence of F127 and charged fatty acid impurities, respectively. In a recent study, it was also reported on the possible production of lamellar and non-lamellar liquid crystalline citrem/soy phosphatidylcholine nanoparticles including cubosomes and hexosomes by using the same low-

energy emulsification method.⁴⁷ In the present work, it was not possible to produce colloiddally stable citrem/MAG-EPA nanoparticles by using this method but rather a high-energy emulsification method had to be applied for their preparation (**Table 1**). Compared to F127, citrem is not a very efficient stabilizer and has to be added in a greater concentration (**Table 1**) but it is attractive for use as a stabilizer as mentioned above owing to the recently reported hemocompatibility and lack of complement activation in citrem-stabilized nanoparticles.^{47,63}

3.4 Effect of Temperature on MAG-EPA Nano-Self Assemblies stabilized by F127. The effect of temperature on MAG-EPA hexosomes stabilized by F127 (sample D_{F127}) was also investigated during a heating-cooling cycle between 5 and 60 °C using a ramp of 1 °C/min. In this study, the selection of F127 instead of citrem as a stabilizer was based on the observed lack influence of F127 on the internal H₂ phase of hexosomes at 37 °C (**Figure 5**). Hence, it was possible to make a direct comparison of the temperature-dependence of MAG-EPA hexosomes with the corresponding fully hydrated non-dispersed bulk H₂ phase at the respective temperatures. **Figure 7A** shows the temperature-induced structural alterations in the internal H₂ phase of hexosomes during heating from 5 to 60 °C. As compared with the fully hydrated bulk sample (**Figure 2C**), the presented X-ray contour plot revealed a similar temperature-dependent behavior with same phase transition sequence: the formation of stable hexosomes with an internal H₂ phase in the temperature range of 5-52.6 °C and a colloidal transition to nanoparticles with a neat L₂ phase (ELP: emulsified L₂ phase) at temperatures above 52.6 °C. The similarity in the phase behaviour of the dispersed and non-dispersed states is most likely attributed to the lack of influence of F127 on the H₂ nanostructure and the occurrence of fast cooperative structural transitions in both the dispersed and non-dispersed phases as stated above. In this context, a similar behavior was observed for MLO dispersions^{31,33} stabilized by F127 that did not have also any influence on the internal

1
2
3
4 nanostructures of the dispersed nanoparticles. It should be noted that the incorporation of F127 into
5
6 the internal nanostructure of the dispersed nanoparticles could be associated with significant
7
8 temperature-induced structural alterations as previously reported for monoelaidin (ME)-based
9
10 dispersion³².
11

12
13 The main difference was the occurrence of the H₂-L₂ phase transition at a slightly lower
14
15 temperature (about 53.5 °C) than that for the corresponding fully hydrated system (about 56 °C). A
16
17 similar behaviour was also reported for MLO dispersion³¹. The exact reason for this phenomenon is
18
19 unclear at present but could be attributed to a greater molecular motion in the dispersed state near
20
21 the H₂-L₂ phase transition region. It seems that the fragmentation of the inverse hexagonal liquid
22
23 crystalline into nanoparticles facilitates the structural transition at a lower temperature by relatively
24
25 enhancing faster molecular re-arrangements in the transition region. In addition to the sample
26
27 environment (nanoparticles vs. fully hydrated bulk liquid crystalline phase), we do not exclude a
28
29 possible role of F127 in facilitating the structural transition.
30
31

32
33 The temperature-dependent behavior of the dispersion during the heating-cooling cycle (**Figures 7B**
34
35 and **7C**) was also very similar to that detected for the fully hydrated sample (**Figures 3 and 4**). As
36
37 illustrated in **Figure 7B**, the reduction in $a(T)$ value of the H₂ phase was almost with same rate of
38
39 about 0.012 nm/°C as the temperature varied in the range of 5-60 °C in both heating and cooling
40
41 steps. It should be noted that a same rate of reduction in $a(T)$ was also detected for the full hydrated
42
43 MAG-EPA system (**Figure 4C**) emphasizing as mentioned above the lack of influence of F127 on
44
45 the H₂ phase. This similarity in the temperature-dependent behaviour between the fully hydrated
46
47 system and the corresponding dispersion is highlighted in **Figure 8** for both H₂ and L₂ phases
48
49 during the heating-cooling cycle. These findings emphasize as mentioned above the lack of
50
51 significant influence of F127 on the internal H₂ and L₂ phases of the dispersed nanoparticles and the
52
53 fast highly cooperative nature of the H₂-L₂ phase transition. The most remarkable difference was
54
55
56
57
58
59
60

the absence of an internal intermediate H_2 phase during heating the dispersion, which was detected at a temperature range of 22-54.5 °C during heating the fully hydrated system. The exact reason is unclear but it could be attributed to relatively faster molecular motions under non-equilibrium conditions in the dispersed nanoparticles with increasing temperature that accelerate the transition from the H_2 phase to the L_2 phase without the occurrence of an intermediate phase.

CONCLUSIONS

Synchrotron SAXS characterization study was conducted to shed light on the effects of hydration and temperature on selected MAG-EPA samples during a heating-cooling cycle in the temperature range of 5-60 °C. At ambient temperatures, the hydration of MAG-EPA induced a transition from an inverse micellar solution (L_2 phase) to a dominant inverse hexagonal (H_2) phase. Our investigations focused on the fragmentation of the detected dominant H_2 phase in excess water for producing hexosomes at room temperature by using either F127 or citrem as a stabilizer. Using different biophysical tools including synchrotron SAXS, NTA, and cryo-TEM, we investigated the structural, size, and morphological characteristics of these colloidal nano-self-assemblies that were stable for at least four months after preparation. F127 did not influence the internal H_2 phase of hexosomes; whereas the use of citrem in a concentration-dependent manner was associated with structural alterations in the interiors of the dispersed nanoparticles. In the performed heating and cooling steps, the obtained SAXS results revealed that the fully hydrated MAG-EPA and its corresponding F127-stabilized dispersion had a very similar behaviour with slight thermal hysteresis indicating insignificant effect of F127 on the internal nanostructure of the dispersed nanoparticles and the occurrence of same fast highly cooperative structural transitions in both the dispersed and non-dispersed (bulk) states.

1
2
3
4
5
6
7
8
9
10
11
12
13
14
15
16
17
18
19
20
21
22
23
24
25
26
27
28
29
30
31
32
33
34
35
36
37
38
39
40
41
42
43
44
45
46
47
48
49
50
51
52
53
54
55
56
57
58
59
60

Taking into consideration the health-promoting effects of MAG-EPA and its possible therapeutic uses in various disorders and the potential use of hexosomes as nanocarriers in drug delivery and bio-imaging applications, it is an attractive strategy in the future to consider a combination of the beneficial health effects of MAG-EPA with loaded therapeutic drugs in the development of multifunctional drug nanocarriers.

ACKNOWLEDGMENTS

Financial support to AY by the Danish Council for Independent Research | Technology and Production Sciences, reference 1335-00150b is gratefully acknowledged. AY further acknowledges financial support from the Danish Natural Sciences Research Council (DanScatt) for SAXS experiments. Special thanks to Dr. Samuel Fortin (SCF Pharma, Quebec, Canada) for fruitful discussions and for providing as a gift MAG-EPA that was synthesized at SCF Pharma.

Table 1: Structure parameters (the lattice parameter, a , for the H_2 phase and the *characteristic distance*, d , for the L_2 -phase) at 37 °C as derived from SAXS investigations presented in **Figure 5** that were carried out on bulk (non-dispersed) MAG-EPA/water systems at different water concentrations and the corresponding three dispersions stabilized by F127 or citrem.

Investigated system	Water content (wt%)	Stabilizer Concentration (wt%)	Phase	a (H_2) (nm)	d (L_2) (nm)
Bulk (non-dispersed): MAG-EPA/water system	5	—	L_2	—	2.88
	15	—	L_2	—	3.58
	40	—	H_2	4.84	—
	40	—	H_2	4.87	—
	90^a	—	H_2	4.87	—
F127-stabilized dispersion (sample D_{F127})	94	1	H_2	4.87	—
Citrem-stabilized dispersion (sample CM2:3)	95	2	H_2	4.91	—
Citrem-stabilized dispersion (sample CM3:2)	95	3	H_2 L_2	5.10 —	— 4.4

^aFully hydrated sample containing 90 wt% water.

Table 2: Size characteristics and zeta potential values for the dispersions stabilized by F127 or citrem as determined at room temperature by NTA, and Zetasizer Nano ZS.

Sample ^a	Size (nm) with standard deviations			Zeta potential (mV)
	Mean	Median	Mode	
D _{F127} : Sonicated F127-stabilized dispersion	82.0 ± 30.3	72.7 ± 30.3	66.3 ± 30.3	-22.70
F127-stabilized dispersion, low-energy ^b	109.1 ± 35.5	93.4 ± 35.5	87.6 ± 35.5	-22.70
CM2:3 ^c	128.7 ± 51.3	115.6 ± 51.3	97.8 ± 51.3	-58.26
CM3:2 ^d	114.3 ± 40.0	104.1 ± 40.0	90.7 ± 40.0	-61.86

^aThe composition of the dispersions and the used stabilizer concentrations are given in Table 1.

^bThe dispersion was prepared using a low-energy emulsification method (vortexing MAG-EPA in excess water for 10 min) at room temperature.

^cThe citrem/MAG-EPA dispersion was prepared at citrem/MAG-EPA weight ratio of 2:3.

^dThe citrem/MAG-EPA dispersion was prepared at citrem/MAG-EPA weight ratio of 3:2.

REFERENCES

1. Kirkhus, B.; Lamglait, A.; Eilertsen, K. E.; Falch, E.; Haider, T.; Vik, H.; Hoem, N.; Hagve, T. A.; Basu, S.; Olsen, E.; Seljeflot, I.; Nyberg, L.; Elind, E.; Ulven, S. M. Effects of Similar Intakes of Marine N-3 Fatty Acids From Enriched Food Products and Fish Oil on Cardiovascular Risk Markers in Healthy Human Subjects. *Br. J. Nutr.* **2012**, *107*, 1339-1349.
2. Maehre, H. K.; Jensen, I. J.; Elvevoll, E. O.; Eilertsen, K. E. Omega-3 Fatty Acids and Cardiovascular Diseases: Effects, Mechanisms and Dietary Relevance. *Int. J. Mol. Sci.* **2015**, *16*, 22636-22661.
3. Calder, P. C. Omega-3 Polyunsaturated Fatty Acids and Inflammatory Processes: Nutrition or Pharmacology? *Br. J. Clin. Pharmacol.* **2013**, *75*, 645-662.
4. Wang, W.; Zhu, J.; Lyu, F.; Panigrahy, D.; Ferrara, K. W.; Hammock, B.; Zhang, G. Omega-3 Polyunsaturated Fatty Acids-Derived Lipid Metabolites on Angiogenesis, Inflammation and Cancer. *Prostaglandins Other Lipid Mediat.* **2014**, *113-115*, 13-20.
5. Bradberry, J. C.; Hilleman, D. E. Overview of Omega-3 Fatty Acid Therapies. *P. T.* **2013**, *38*, 681-691.
6. Souza, P. R.; Norling, L. V. Implications for Eicosapentaenoic Acid- and Docosahexaenoic Acid-Derived Resolvins As Therapeutics for Arthritis. *Eur. J. Pharmacol.* **2016**, *785*, 165-173.
7. Mozaffarian, D.; Wu, J. H. (n-3) Fatty Acids and Cardiovascular Health: Are Effects of EPA and DHA Shared or Complementary? *J. Nutr.* **2012**, *142*, 614S-625S.
8. Byelashov, O. A.; Sinclair, A. J.; Kaur, G. Dietary Sources, Current Intakes, and Nutritional Role of Omega-3 Docosapentaenoic Acid. *Lipid Technol.* **2015**, *27*, 79-82.
9. Harris, W. S.; Kris-Etherton, P. M.; Harris, K. A. Intakes of Long-Chain Omega-3 Fatty Acid Associated With Reduced Risk for Death From Coronary Heart Disease in Healthy Adults. *Curr. Atheroscler. Rep.* **2008**, *10*, 503-509.
10. Domingo, J. L.; Bocio, A.; Falco, G.; Llobet, J. M. Benefits and Risks of Fish Consumption Part I. A Quantitative Analysis of the Intake of Omega-3 Fatty Acids and Chemical Contaminants. *Toxicology* **2007**, *230*, 219-226.
11. Hadian, Z. A Review of Nanoliposomal Delivery System for Stabilization of Bioactive Omega-3 Fatty Acids. *Electron Physician* **2016**, *8*, 1776-1785.
12. Sahari, M. A.; Moghimi, H. R.; Hadian, Z.; Barzegar, M.; Mohammadi, A. Physicochemical Properties and Antioxidant Activity of Alpha-Tocopherol Loaded Nanoliposome's Containing DHA and EPA. *Food Chem.* **2017**, *215*, 157-164.
13. Murru, E.; Banni, S.; Carta, G. Nutritional Properties of Dietary Omega-3-Enriched Phospholipids. *Biomed. Res. Int.* **2013**, *2013*, 965417.
14. Davidson, M. H.; Johnson, J.; Rooney, M. W.; Kyle, M. L.; Kling, D. F. A Novel Omega-3 Free Fatty Acid Formulation Has Dramatically Improved Bioavailability During a Low-Fat Diet Compared With Omega-3-Acid Ethyl Esters: the ECLIPSE (Epanova(R)) Compared to Lovaza(R)) in a Pharmacokinetic Single-Dose Evaluation) Study. *J. Clin. Lipidol.* **2012**, *6*, 573-584.
15. Davidson, M. H.; Benes, L. B. The Future of N-3 Polyunsaturated Fatty Acid Therapy. *Curr. Opin. Lipidol.* **2016**, *27*, 570-578.

16. Dyerberg, J.; Madsen, P.; Moller, J. M.; Aardestrup, I.; Schmidt, E. B. Bioavailability of Marine N-3 Fatty Acid Formulations. *Prostaglandins Leukot. Essent. Fatty Acids* **2010**, *83*, 137-141.
17. Fortin, S. Compositions Comprising Polyunsaturated Fatty Acid Monoglycerides or Derivatives Thereof and Uses Thereof. *US patents* **2012**, 819690 and 8222295.
18. Fortin, S. Polyunsaturated Fatty Acid Monoglycerides, Derivatives, and Uses Thereof. *US patent* **2012**, 8119690.
19. Khaddaj-Mallat, R.; Morin, C.; Rousseau, E. Novel N-3 PUFA Monoacylglycerides of Pharmacological and Medicinal Interest: Anti-Inflammatory and Anti-Proliferative Effects. *Eur. J. Pharmacol.* **2016**, *792*, 70-77.
20. Morin, C.; Fortin, S.; Cantin, A. M.; Rousseau, E. MAG-EPA Resolves Lung Inflammation in an Allergic Model of Asthma. *Clin. Exp. Allergy* **2013**, *43*, 1071-1082.
21. Morin, C.; Fortin, S.; Cantin, A. M.; Sirois, M.; Sirois, C.; Rizcallah, E.; Rousseau, E. Anti-Cancer Effects of a New Docosahexaenoic Acid Monoacylglyceride in Lung Adenocarcinoma. *Recent Pat Anticancer Drug Discov.* **2013**, *8*, 319-334.
22. Morin, C.; Hiram, R.; Rousseau, E.; Blier, P. U.; Fortin, S. Docosapentaenoic Acid Monoacylglyceride Reduces Inflammation and Vascular Remodeling in Experimental Pulmonary Hypertension. *Am. J. Physiol. Heart Circ. Physiol.* **2014**, *307*, H574-H586.
23. Morin, C.; Blier, P. U.; Fortin, S. Eicosapentaenoic Acid and Docosapentaenoic Acid Monoglycerides Are More Potent Than Docosahexaenoic Acid Monoglyceride to Resolve Inflammation in a Rheumatoid Arthritis Model. *Arthritis Res. Ther.* **2015**, *17*, 142.
24. Morin, C.; Rousseau, E.; Blier, P. U.; Fortin, S. Effect of Docosahexaenoic Acid Monoacylglyceride on Systemic Hypertension and Cardiovascular Dysfunction. *Am. J. Physiol. Heart Circ. Physiol.* **2015**, *309*, H93-H102.
25. Morin, C.; Blier, P. U.; Fortin, S. MAG-EPA Reduces Severity of DSS-Induced Colitis in Rats. *Am. J. Physiol. Gastrointest. Liver Physiol.* **2016**, *310*, G808-G821.
26. Morin, C.; Charbonneau, L.; Ouellet, N.; Ouellet, H.; Blier, P. U.; Dufresne, F.; Fortin, S. Eicosapentaenoic Acid Monoglyceride Resolves Inflammation in an Ex Vivo Model of Human Peripheral Blood Mononuclear Cell. *Eur. J. Pharmacol.* **2017**, *807*, 205-211.
27. Cruz-Hernandez, C.; Thakkar, S. K.; Moulin, J.; Oliveira, M.; Masserey-Elmelegy, I.; Dionisi, F.; Destailats, F. Benefits of Structured and Free Monoacylglycerols to Deliver Eicosapentaenoic (EPA) in a Model of Lipid Malabsorption. *Nutrients*. **2012**, *4*, 1781-1793.
28. Morin, C.; Rousseau, E.; Fortin, S. Anti-Proliferative Effects of a New Docosapentaenoic Acid Monoacylglyceride in Colorectal Carcinoma Cells. *Prostaglandins Leukot. Essent. Fatty Acids* **2013**, *89*, 203-213.
29. Qiu, H.; Caffrey, M. The Phase Diagram of the Monoolein/Water System: Metastability and Equilibrium Aspects. *Biomaterials* **2000**, *21*, 223-234.
30. Yaghmur, A.; Sartori, B.; Rappolt, M. Self-Assembled Nanostructures of Fully Hydrated Monoelaidin-Elaidic Acid and Monoelaidin-Oleic Acid Systems. *Langmuir* **2012**, *28*, 10105-10119.
31. de Campo, L.; Yaghmur, A.; Sagalowicz, L.; Leser, M. E.; Watzke, H.; Glatter, O. Reversible Phase Transitions in Emulsified Nanostructured Lipid Systems. *Langmuir* **2004**, *20*, 5254-5261.

32. Yaghmur, A.; Laggner, P.; Almgren, M.; Rappolt, M. Self-Assembly in Monoelaidin Aqueous Dispersions: Direct Vesicles to Cubosomes Transition. *PLoS ONE* **2008**, *3*, e3747.
33. Yaghmur, A.; Glatter, O. Characterization and Potential Applications of Nanostructured Aqueous Dispersions. *Adv. Colloid Interface Sci.* **2009**, *147-148*, 333-342.
34. Czeslik, C.; Winter, R.; Rapp, G.; Bartels, K. Temperature- and Pressure-Dependent Phase Behavior of Monoacylglycerides Monoolein and Monoelaidin. *Biophys. J.* **1995**, *68*, 1423-1429.
35. Shearman, G. C.; Ces, O.; Templer, R. H.; Seddon, J. M. Inverse Lyotropic Phases of Lipids and Membrane Curvature. *J. Phys.-Condens. Mat.* **2006**, *18*, S1105-S1124.
36. Fong, C.; Le, T.; Drummond, C. J. Lyotropic Liquid Crystal Engineering-Ordered Nanostructured Small Molecule Amphiphile Self-Assembly Materials by Design. *Chem. Soc. Rev.* **2012**, *41*, 1297-1322.
37. Kulkarni, C. V.; Wachter, W.; Iglesias-Salto, G.; Engelskirchen, S.; Ahualli, S. Monoolein: a Magic Lipid? *Phys. Chem. Chem. Phys.* **2011**, *13*, 3004-3021.
38. Chung, H.; Caffrey, M. Polymorphism, Mesomorphism, and Metastability of Monoelaidin in Excess Water. *Biophys. J.* **1995**, *69*, 1951-1963.
39. Azmi, I. D.; Moghimi, S. M.; Yaghmur, A. Cubosomes and Hexosomes As Versatile Platforms for Drug Delivery. *Ther. Deliv.* **2015**, *6*, 1347-1364.
40. van 't, H. L.; Gras, S. L.; Conn, C. E.; Drummond, C. J. Lyotropic Liquid Crystal Engineering Moving Beyond Binary Compositional Space - Ordered Nanostructured Amphiphile Self-Assembly Materials by Design. *Chem. Soc. Rev.* **2017**, *46*, 2705-2731.
41. Fong, W. K.; Negrini, R.; Vallooran, J. J.; Mezzenga, R.; Boyd, B. J. Responsive Self-Assembled Nanostructured Lipid Systems for Drug Delivery and Diagnostics. *J. Colloid Interface Sci.* **2016**, *484*, 320-339.
42. Larsson, K. Aqueous Dispersions of Cubic Lipid-Water Phases. *Curr. Opin. Colloid Interface Sci.* **2000**, *5*, 64-69.
43. Nilsson, C.; Barrios-Lopez, B.; Kallinen, A.; Laurinmaki, P.; Butcher, S. J.; Raki, M.; Weisell, J.; Bergstrom, K.; Larsen, S. W.; Ostergaard, J.; Larsen, C.; Urtti, A.; Airaksinen, A. J.; Yaghmur, A. SPECT/CT Imaging of Radiolabeled Cubosomes and Hexosomes for Potential Theranostic Applications. *Biomaterials* **2013**, *34*, 8491-8503.
44. Angelova, A.; Garamus, V. M.; Angelov, B.; Tian, Z.; Li, Y.; Zou, A. Advances in Structural Design of Lipid-Based Nanoparticle Carriers for Delivery of Macromolecular Drugs, Phytochemicals and Anti-Tumor Agents. *Adv. Colloid Interface Sci.* **(In Press)**.
45. Tran, N.; Bye, N.; Moffat, B. A.; Wright, D. K.; Cuddihy, A.; Hinton, T. M.; Hawley, A. M.; Reynolds, N. P.; Waddington, L. J.; Mulet, X.; Turnley, A. M.; Morganti-Kossmann, M. C.; Muir, B. W. Dual-Modality NIRF-MRI Cubosomes and Hexosomes: High Throughput Formulation and in Vivo Biodistribution. *Mater. Sci. Eng. C Mater. Biol. Appl.* **2017**, *71*, 584-593.
46. Meli, V.; Caltagirone, C.; Falchi, A. M.; Hyde, S. T.; Lippolis, V.; Monduzzi, M.; Obiols-Rabasa, M.; Rosa, A.; Schmidt, J.; Talmon, Y.; Murgia, S. Docetaxel-Loaded Fluorescent Liquid-Crystalline Nanoparticles for Cancer Theranostics. *Langmuir* **2015**, *31*, 9566-9575.
47. Azmi, I. D.; Wibroe, P. P.; Wu, L. P.; Kazem, A. I.; Amenitsch, H.; Moghimi, S. M.; Yaghmur, A. A Structurally Diverse Library of Safe-by-Design Citrem-Phospholipid

- Lamellar and Non-Lamellar Liquid Crystalline Nano-Assemblies. *J. Control. Release* **2016**, *239*, 1-9.
48. Briggs, J.; Caffrey, M. The Temperature-Composition Phase Diagram and Mesophase Structure Characterization of Monopentadecenoin in Water. *Biophys. J.* **1994**, *67*, 1594-1602.
49. Briggs, J.; Chung, H.; Caffrey, M. The Temperature-Composition Phase Diagram and Mesophase Structure Characterization of the Monoolein/Water System. *J. Phys. II* **1996**, *6*, 723-751.
50. Qiu, H.; Caffrey, M. Phase Behavior of the Monoerucin/Water System. *Chem. Phys. Lipids* **1999**, *100*, 55-79.
51. Lutton, E. S. Phase Behavior of Aqueous Systems of Monoglycerides. *J. Am. Oil Chem. Soc.* **1965**, *42*, 1068-1070.
52. Qiu, H.; Caffrey, M. Lyotropic and Thermotropic Phase Behavior of Hydrated Monoacylglycerols: Structure Characterization of Monovaccenin. *J. Phys. Chem. B* **1998**, *102*, 4819-4829.
53. Yaghmur, A.; de Campo, L.; Sagalowicz, L.; Leser, M. E.; Glatter, O. Control of the Internal Structure of MLO-Based Isosomes by the Addition of Diglycerol Monooleate and Soybean Phosphatidylcholine. *Langmuir* **2006**, *22*, 9919-9927.
54. Johnsson, M.; Lam, Y.; Barauskas, J.; Tiberg, F. Aqueous Phase Behavior and Dispersed Nanoparticles of Diglycerol Monooleate/Glycerol Dioleate Mixtures. *Langmuir* **2005**, *21*, 5159-5165.
55. Lee, W. B.; Mezzenga, R.; Fredrickson, G. H. Self-Consistent Field Theory for Lipid-Based Liquid Crystals: Hydrogen Bonding Effect. *J. Chem. Phys.* **2008**, *128*, 074504.
56. Shearman, G. C.; Tyler, A. I. I.; Brooks, N. J.; Templar, R. H.; Ces, O.; Law, R. V.; Seddon, J. M. Ordered Micellar and Inverse Micellar Lyotropic Phases. *Liquid Crystals* **2010**, *37*, 679-694.
57. Briggs, J.; Caffrey, M. The Temperature-Composition Phase Diagram of Monomyristolein in Water: Equilibrium and Metastability Aspects. *Biophys. J.* **1994**, *66*, 573-587.
58. Mezzenga, R.; Meyer, C.; Servais, C.; Romoscanu, A. I.; Sagalowicz, L.; Hayward, R. C. Shear Rheology of Lyotropic Liquid Crystals: A Case Study. *Langmuir* **2005**, *21*, 3322-3333.
59. Tenchov, B. On the Reversibility of the Phase Transitions in Lipid-Water Systems. *Chem. Phys. Lipids* **1991**, *57*, 165-177.
60. Yaghmur, A.; Laggner, P.; Zhang, S.; Rappolt, M. Tuning Curvature and Stability of Monoolein Bilayers by Designer Lipid-Like Peptide Surfactants. *PLoS ONE* **2007**, *2*, e479.
61. Gustafsson, J.; Ljusberg-Wahren, H.; Almgren, M.; Larsson, K. Submicron Particles of Reversed Lipid Phases in Water Stabilized by a Nonionic Amphiphilic Polymer. *Langmuir* **1997**, *13*, 6964-6971.
62. Kulkarni, C. V.; Yaghmur, A.; Steinhart, M.; Kriechbaum, M.; Rappolt, M. Effects of High Pressure on Internally Self-Assembled Lipid Nanoparticles: A Synchrotron Small-Angle X-Ray Scattering (SAXS) Study. *Langmuir* **2016**, *32*, 11907-11917.
63. Wibroe, P. P.; Mat Azmi, I. D.; Nilsson, C.; Yaghmur, A.; Moghimi, S. M. Citrem Modulates Internal Nanostructure of Glyceryl Monooleate Dispersions and Bypasses Complement Activation: Towards Development of Safe Tunable Intravenous Lipid Nanocarriers. *Nanomedicine*. **2015**, *11*, 1909-1914.

64. Nakano, M.; Teshigawara, T.; Sugita, A.; Leesajakul, W.; Taniguchi, A.; Kamo, T.; Matsuoka, H.; Handa, T. Dispersions of Liquid Crystalline Phases of the Monoolein/Oleic Acid/Pluronic F127 System. *Langmuir* **2002**, *18*, 9283-9288.
65. Nilsson, C.; Edwards, K.; Eriksson, J.; Larsen, S. W.; Ostergaard, J.; Larsen, C.; Urtti, A.; Yaghmur, A. Characterization of Oil-Free and Oil-Loaded Liquid-Crystalline Particles Stabilized by Negatively Charged Stabilizer Citrem. *Langmuir* **2012**, *28*, 11764-11775.
66. Hedegaard, S. F.; Nilsson, C.; Laurinmaki, P.; Butcher, S.; Urtti, A.; Yaghmur, A. Aqueous Dispersions of the Oil-Soluble Anionic Surfactant Citrem Interacting With Lipids and PEGylated Lipids. *RSC Adv.* **2013**, *3*, 24576-24585.
67. Khaliqi, K.; Ghazal, A.; Azmi, I. D. M.; Amenitsch, H.; Mortensen, K.; Salentinig, S.; Yaghmur, A. Direct Monitoring of Lipid Transfer on Exposure of Citrem Nanoparticles to an Ethanol Solution Containing Soybean Phospholipids by Combining Synchrotron SAXS With Microfluidics. *Analyst* **2017**, *142*, 3118-3126.
68. Berton, C.; Genot, C.; Ropers, M. H. Quantification of Unadsorbed Protein and Surfactant Emulsifiers in Oil-in-Water Emulsions. *J. Colloid Interface Sci.* **2011**, *354*, 739-748.
69. Spicer, P. T.; Hayden, K. L.; Lynch, M. L.; Ofori-Boateng, A.; Burns, J. L. Novel Process for Producing Cubic Liquid Crystalline Nanoparticles (Cubosomes). *Langmuir* **2001**, *17*, 5748-5756.

FIGURE CAPTIONS

Figure 1. The molecular structure of ω -3 PUFAs and their corresponding ω -3 monoglycerides: eicosapentaenoic acid (EPA; 20:5 n-3), docosahexaenoic acid (DHA; 22:6 n-3), docosapentaenoic acid (DPA; 22:5 n-3), eicosapentaenoic acid (MAG-EPA), docosahexaenoic acid (MAG-DHA), and docosapentaenoic acid (MAG-DPA) monoglycerides.

Figure 2. The temperature-dependent behaviour of the three hydrated MAG-EPA-based systems containing 5 (panel A), 15 (panel B), and 90 wt% water (panel C). The first two samples were transparent solutions prepared under limited hydration conditions; whereas the sample containing 90 wt% water was fully hydrated. In the temperature range of 5-60 °C, the heating scan rate was 1 °C/min and T-scan patterns were recorded every a degree. The X-ray contour plots for these experiments are given in panels (A), (B), and (C), respectively. The SAXS profiles are given along the z-axis.

Figure 3. Representative SAXS patterns for the temperature-dependent behaviour of the three hydrated MAG-EPA-based systems containing 5 (panel A), 15 (panel B), and 90 wt% water (panel C) during the heating-cooling cycle in the temperature range of 5-60 °C and a scan rate of 1 °C/min. In the heating direction, the selected patterns at different temperatures (black lines) refer to SAXS data presented in **Figure 2** and are compared with those taken at same temperatures during cooling the samples (red lines).

Figure 4. Variation in the characteristic distance and the unit cell parameter as a function of temperature for the L₂ and H₂ phases, respectively. The data for the hydrated MAG-EPA-based systems containing 5 wt% water (panel A), 15 wt% water (panel B), and 90 wt% water (panel C) during the heating-cooling cycle are extracted from the SAXS experiments displayed in **Figure 2** in the heating step, and also from those performed during cooling. During the heating step, the L₂ and

H₂ phases are represented by full black circles and full olive colored squares, respectively; whereas they are represented by open red circles, and open olive colored squares during the cooling step. It should be noted that the intermediate H₂ phase detected under full hydration conditions is represented by inverted full triangles (panel C). This intermediate phase was stable in the temperature range of 22-54.5 °C but we were able to calculate its lattice parameter in the following temperature ranges: 22-25 °C and 46-54.5 °C. Thus, the lattice parameters are not given between 25 and 46 °C and also in the cooling step as the peaks of both coexisting phases are overlapped, which is made it not possible to identify the characteristic reflections of the intermediate H₂ phase.

Figure 5. (A) Structural characterization of three ultrasonicated MAG-EPA-based dispersions: a dispersion stabilized by F127 and two dispersions prepared at two different citrem/ MAG-EPA (CM) weight ratios: 3:2 and 2:3. (B) Comparison of the SAXS pattern of F127-stabilized dispersion with those of the bulk (non-dispersed) phases prepared at different water content. The three dispersions were prepared at same lipid (MAG-EPA or citrem/MAG-EPA) concentration of 5 wt%. The SAXS experiments were performed at 37 °C and the intensities have been shifted by a constant arbitrary factor for better visibility.

Figure 6. Cryo-TEM micrographs of three ultrasonicated MAG-EPA-based dispersions: a dispersion stabilized by F127 (A) and two dispersions prepared at two different citrem/ MAG-EPA (CM) weight ratios of 3:2 (B) and 2:3 (C). Scale bars: 200 nm. The micrographs of F127-stabilized dispersion (A) revealed the formation of nanoparticles enveloping an internal nanostructure coexisting with vesicles (marked with an arrow); whereas the micrographs of CM dispersions (panels (B) and (C)) did not show any indication on the formation of vesicles.

Figure 7. (A) The SAXS contour plot for the ultrasonicated MAG-EPA-based dispersion that was stabilized by F127. The temperature-dependent behaviour was investigated in the temperature range

of 5-60 °C. The heating scan rate was 1 °C/min and T-scan patterns were recorded every a degree. The SAXS profiles are given along the z-axis. (B) Variation in the characteristic distance and the unit cell parameter as a function of temperature for the internal L₂ and H₂ phases, respectively. The data are extracted from the SAXS experiments performed during the heating-cooling cycle. (C) Representative SAXS patterns for the temperature-dependent behaviour of the ultrasonicated MAG-EPA dispersion during the heating-cooling cycle. In the heating direction, the selected patterns at different temperatures (black lines) are compared with those taken at same temperatures during cooling the samples (red lines).

Figure 8. Variation in the characteristic distance and the unit cell parameter as a function of temperature for the internal L₂ and H₂ phases of F127-stabilized dispersion as compared to the fully hydrated bulk (non-dispersed) sample. The change in the lattice parameter of the H₂ phase is given during heating (A) and cooling (B) steps. The change in the characteristic distance, d , for the L₂ phase is given in panels (C) and (D) during the heating and cooling steps, respectively. The data were extracted from the performed SAXS experiments during the heating-cooling cycle.

Figure 1

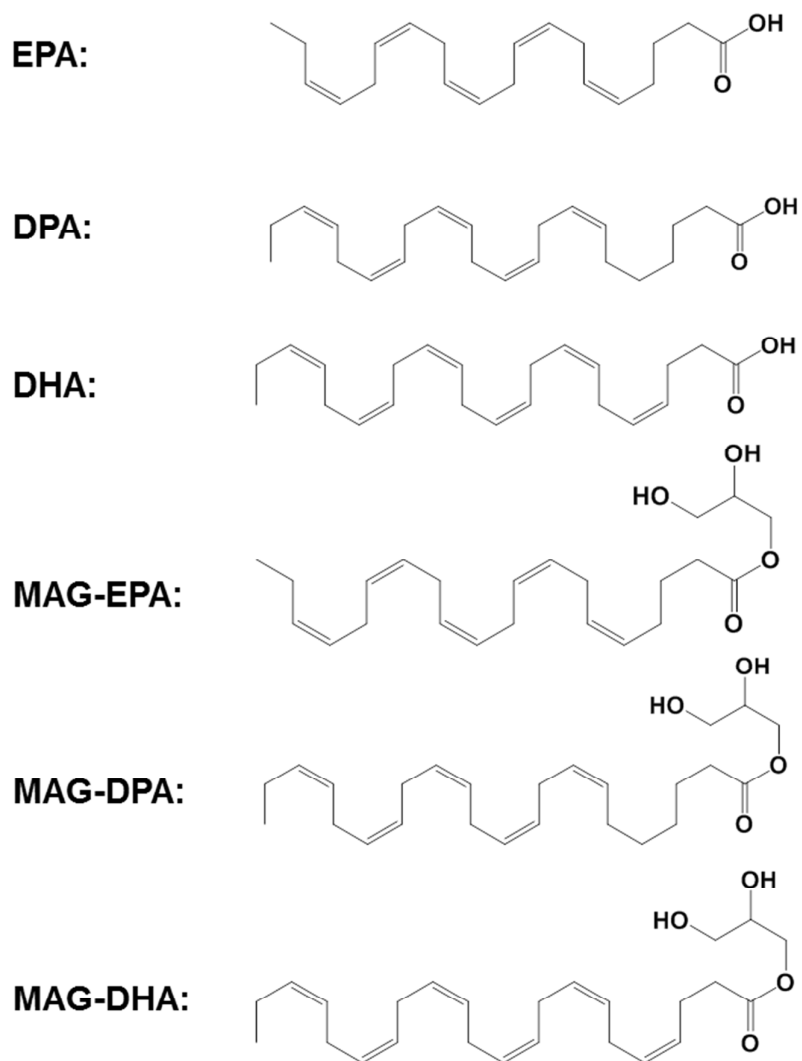


Figure 2

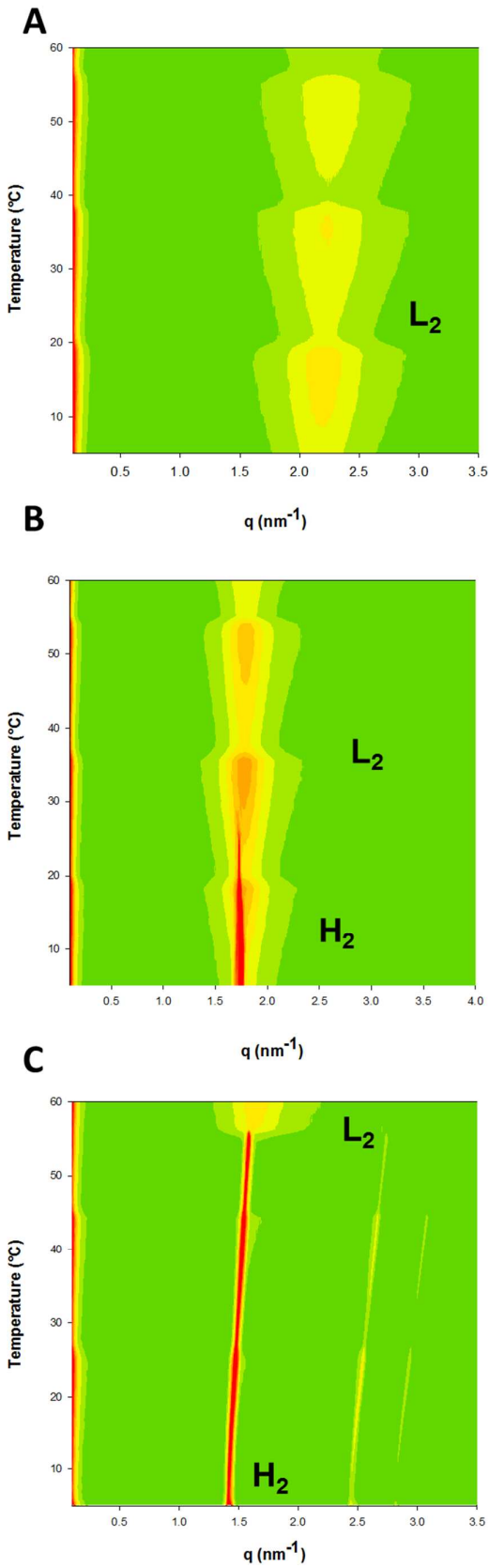


Figure 3

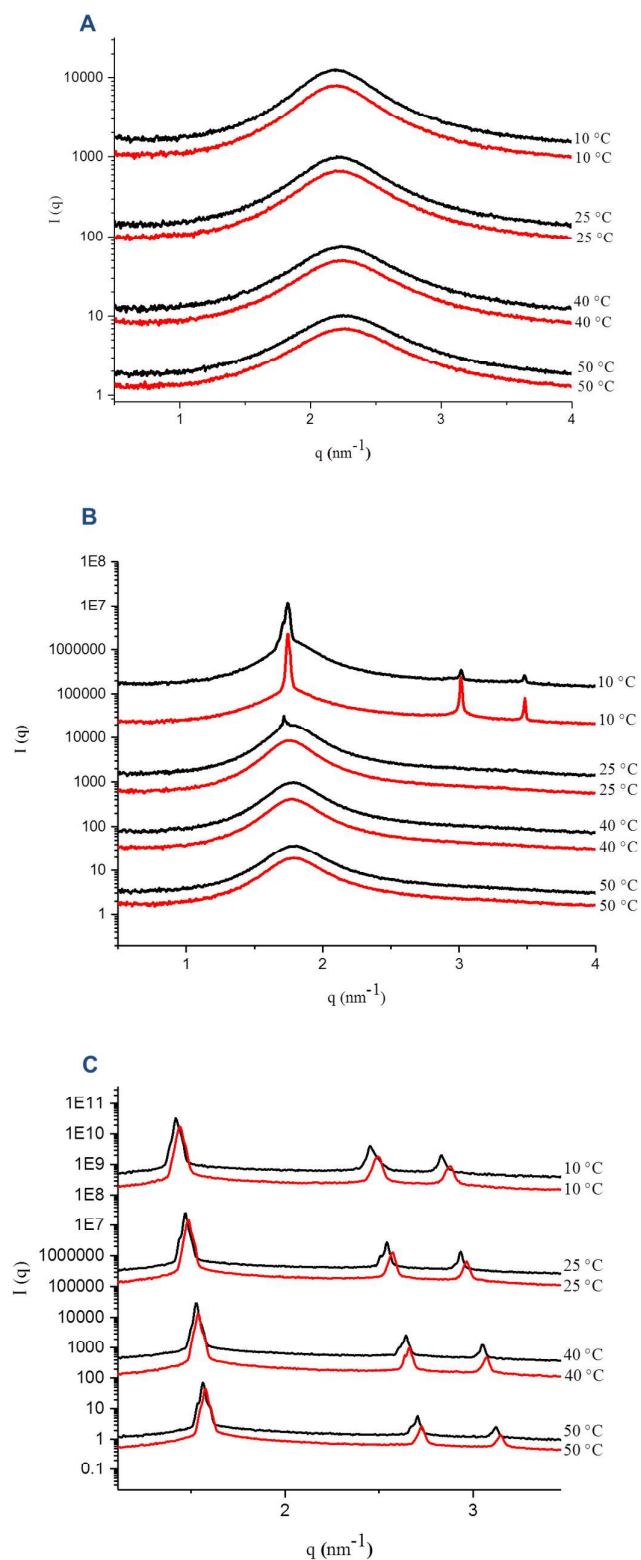


Figure 4

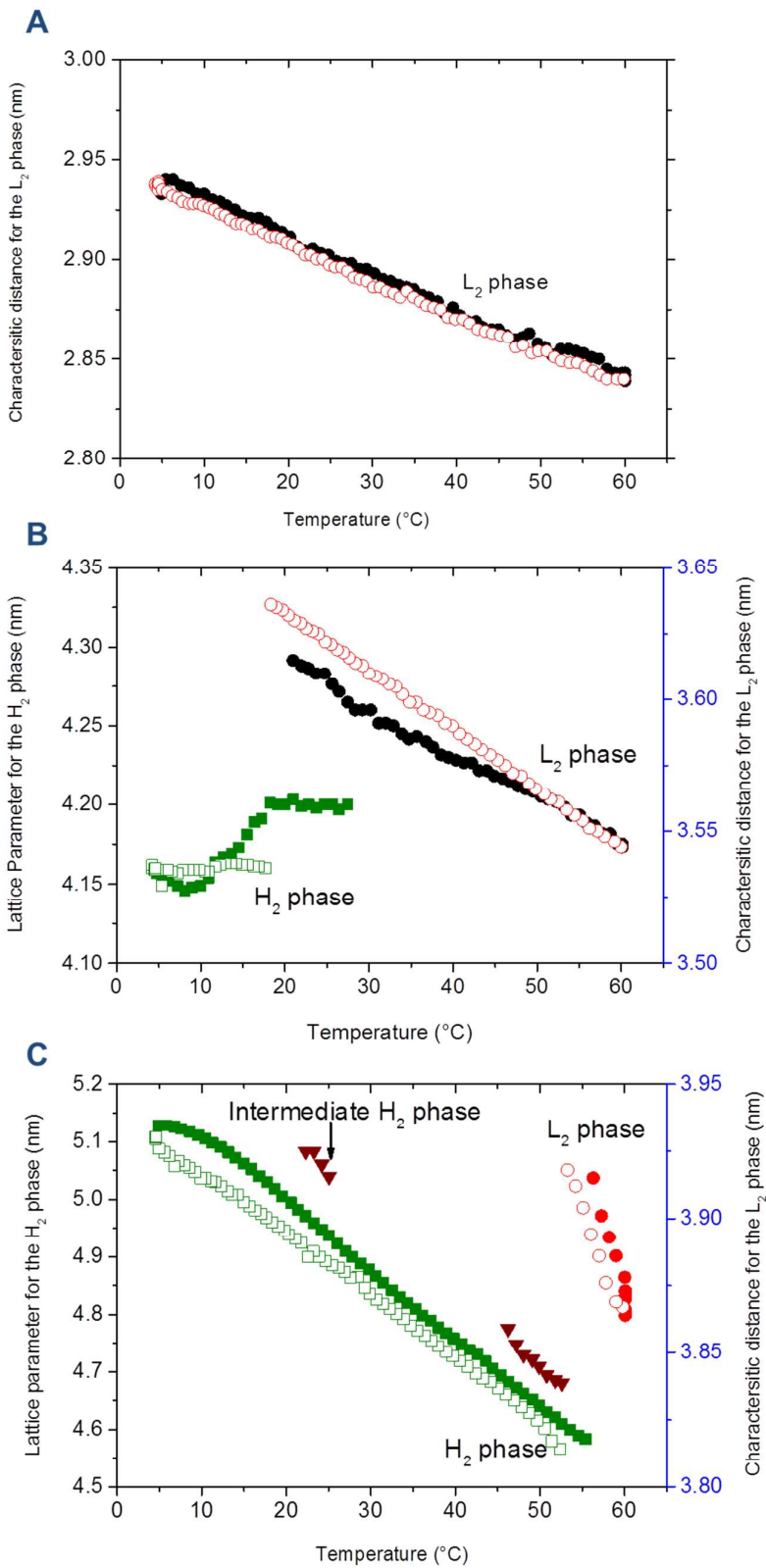


Figure 5

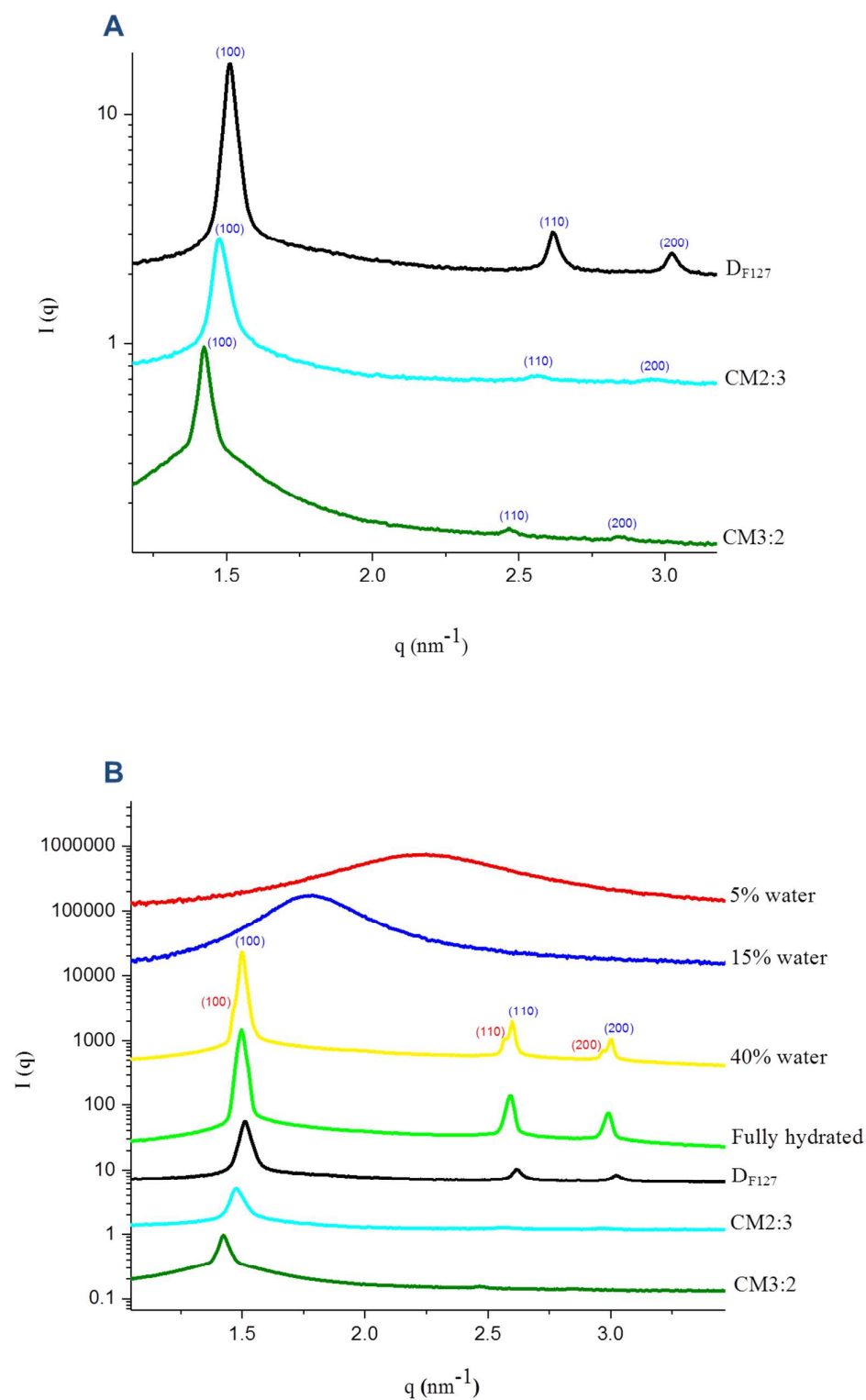


Figure 6

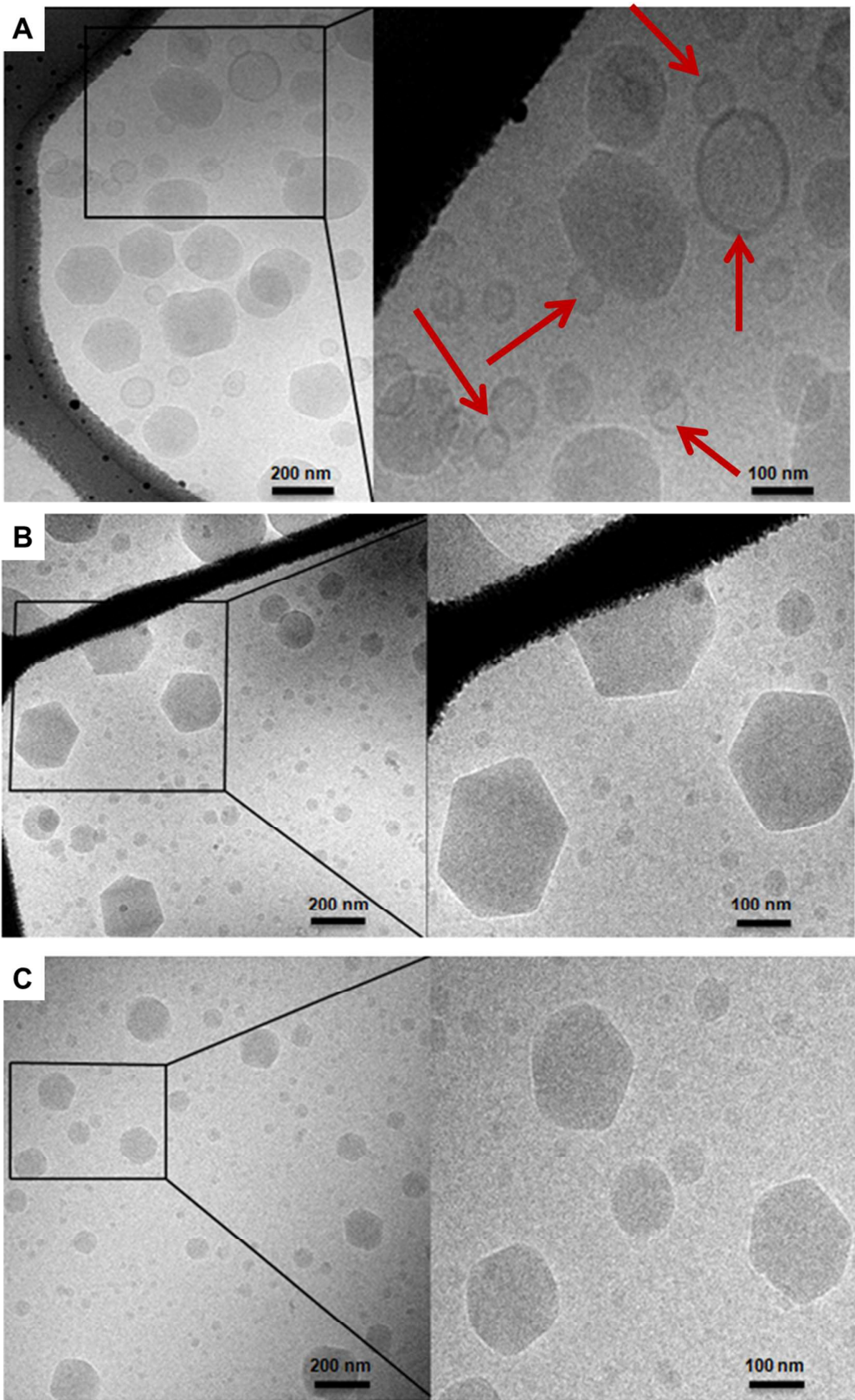
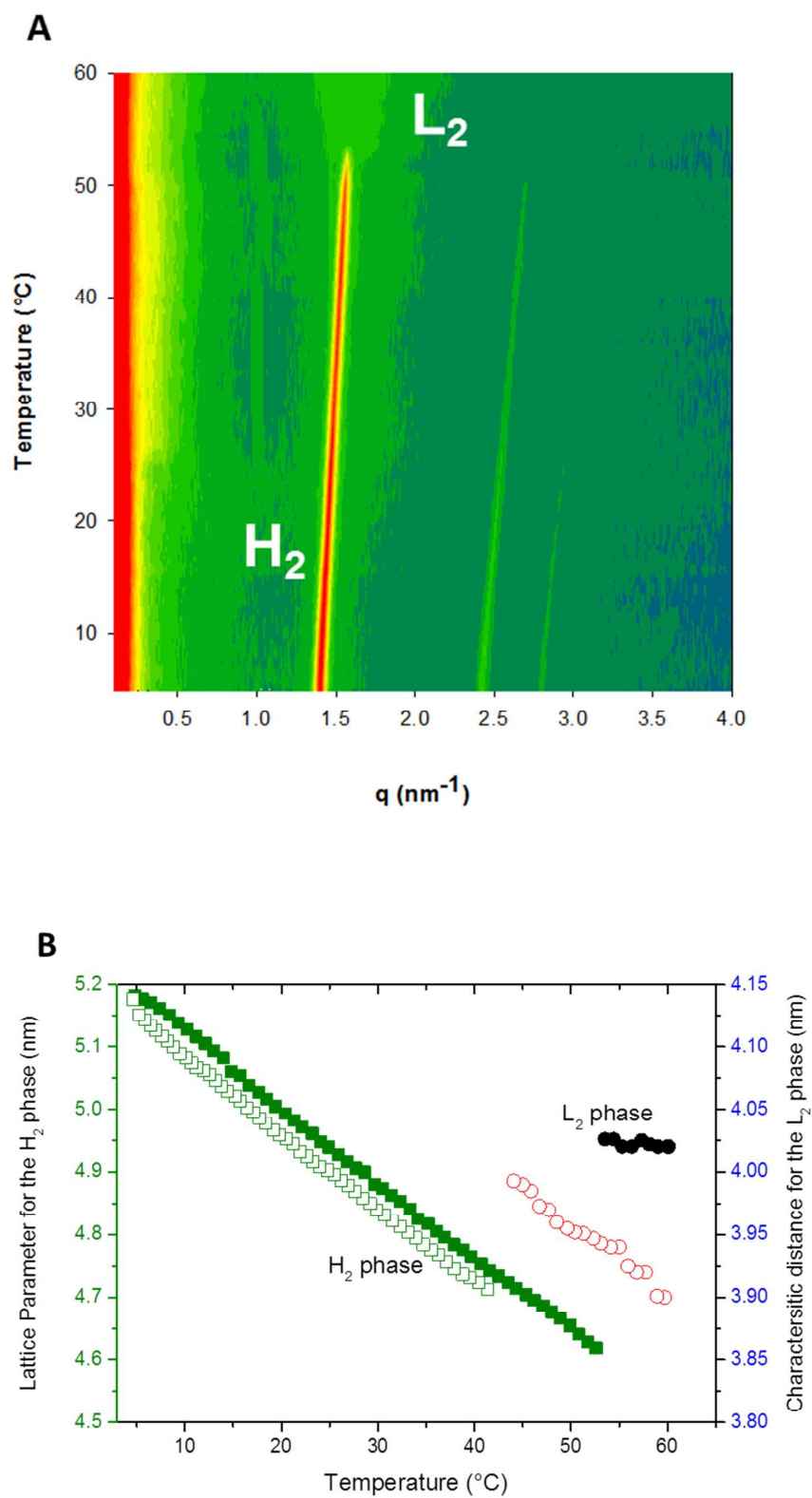


Figure 7



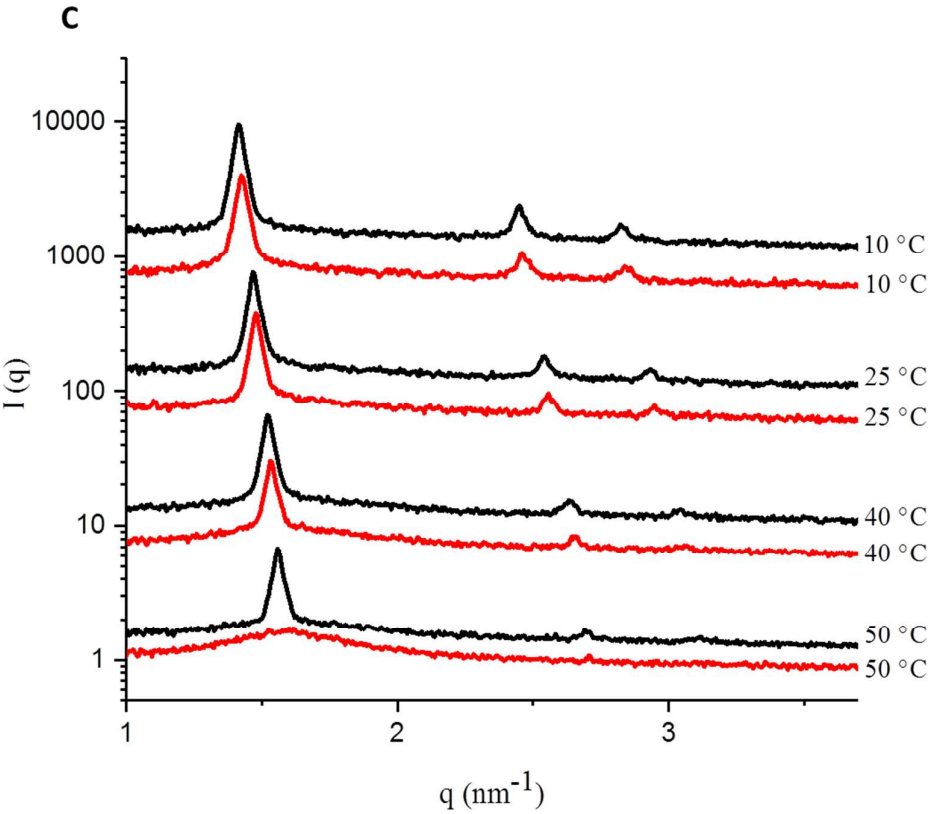
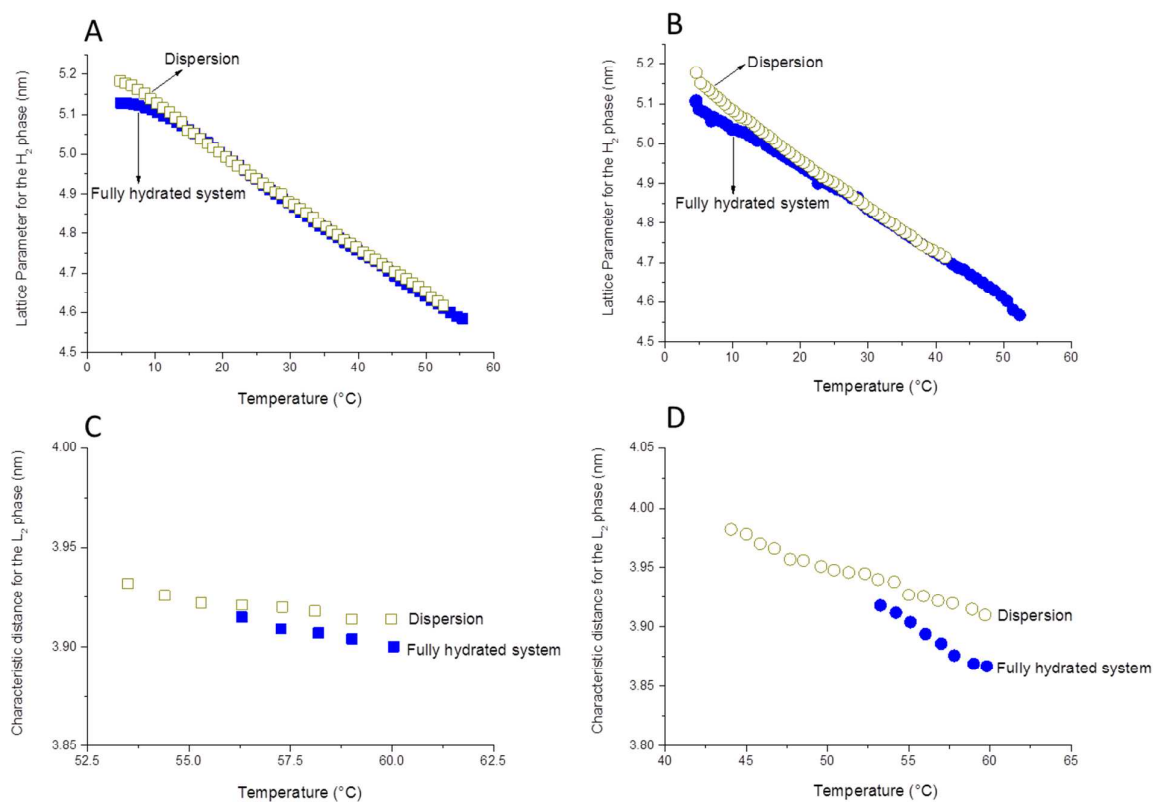
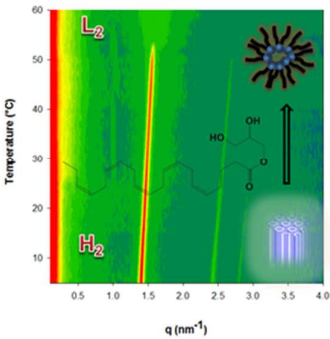
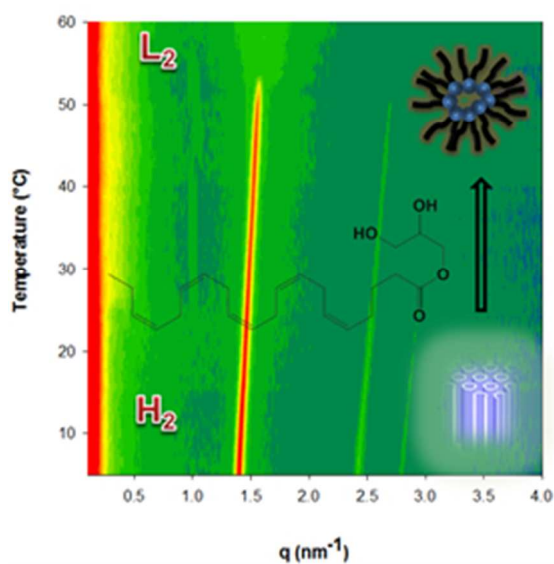


Figure 8



TOC





Characterization of MAG-EPA Nano-Self-Assemblies: experimental synchrotron SAXS evidence on the temperature-induced transition from hexosomes with an internal inverse hexagonal (H_2) liquid crystalline phase to nanoparticles with an internal neat L_2 phase (ELP: emulsified L_2 phase). The SAXS profiles are given along the z-axis.

Graphic for

48x49mm (150 x 150 DPI)